Nano Research

Open Access

Research Article

Suppressing back-interface recombination in CZTSSe solar cells via SiO_2 nanoparticle-induced discrete local contacts

Yuanyuan Huang[1,2], Yu Mao[1,2], Yanmei Deng[1,2], Mengyang Wang[1,2], Wenjian Chan[1,2], Ziyang Ren[1,2], Ening Gu[3], Xianzhong Lin[1,2] ✉, and Guowei Yang[1]

[1] *Guangzhou Key Laboratory of Flexible Electronic Materials and Wearable Devices, State Key Laboratory of Optoelectronic Materials and Technologies, Nanotechnology Research Center, School of Materials Science and Engineering, Sun Yat-Sen University, Guangzhou 510275, China*

[2] *Key Laboratory of Polymeric Composite and Functional Materials of Ministry of Education, Sun Yat-Sen University, Guangzhou 510275, China*

[3] *School of Materials and Energy, Foshan University, Foshan 528231, China*

Cite this article: *Nano Research*, **2025**, *18*, 94907907. https://doi.org/10.26599/NR.2025.94907907

ABSTRACT: The severe back interface recombination remains a major performance limiting factor in $Cu_2ZnSn(S,Se)_4$ (CZTSSe) solar cells. In this work, SiO_2 nanoparticles deposited on Mo substrate by spin-coating were used to create discrete local contact points to passivate the back interface. Systematic investigation of nanoparticle size reveals that optimized SiO_2 incorporation enhances absorber crystallinity, reduces interfacial defect density, and suppresses detrimental [$2Cu_{Zn}$ + Sn_{Zn}] deep-level clusters. Meanwhile, it can effectively inhibit nanoparticle agglomeration while maintaining optimal hole-transport distances, thereby obtaining a more efficient porous insulator contact (PIC) passivation structure. We propose that the passivation mechanism involves carrier recombination suppression through minimized defective contact area, thus improving the back contact quality. Consequently, the power conversion efficiency of the ultrathin CZTSSe solar cells increases from 9.03% to 10.72%, offering a viable approach for back-contact engineering.

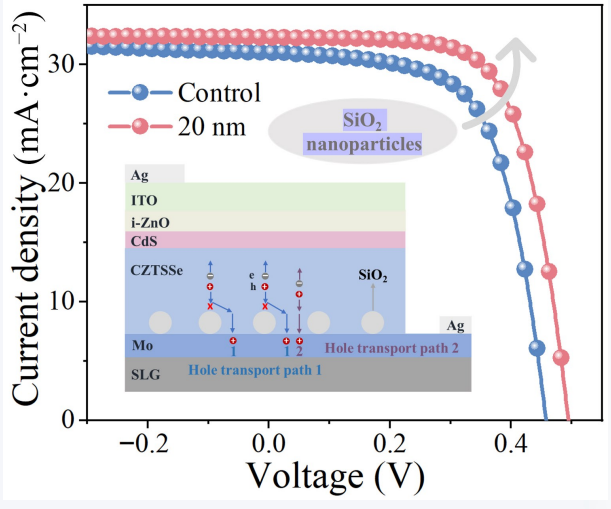

KEYWORDS: $Cu_2ZnSn(S,Se)_4$ (CZTSSe) solar cells, discrete local contact, SiO_2 nanoparticles, back interface passivation

1 Introduction

Kesterite $Cu_2ZnSn(S,Se)_4$ (CZTSSe), as a promising next-generation photovoltaic material, has emerged as a critical research direction in the photovoltaic field due to its environmental friendliness, abundant elemental resources, strong light-absorption capability, and excellent stability [1–5]. Although significant progress has been made in improving their power conversion efficiency (PCE) in recent years, the efficiency remains far below the Shockley–Queisser theoretical limit of 33.0% [6], primarily constrained by bottlenecks in enhancing the open-circuit voltage (V_{OC}) and fill factor (FF) [7]. Due to issues, such as energy level matching and interfacial defects, CZTSSe solar cells suffer from poor carrier transport capability caused by severe interfacial recombination [8]. The poor contact at the Mo/CZTSSe back interface is one of the key limiting factors: during high-temperature selenization, insufficient thermodynamic stability at the interface leads to the formation of secondary phases, deep-level defects, and void structures, increasing interface contact resistance and carrier recombination, thereby significantly impacting V_{OC} and FF [9, 10].

To address the back-interface contact problem, a strategy of introducing an intermediate layer at the Mo/CZTSSe back interface has been adopted [11]. Kim et al. prepared an ultra-thin Al_2O_3 passivation layer using atomic layer deposition technology, which effectively prevented the formation of $MoSe_2$ and improved the back contact quality [12]. Liang et al. regulated the crystal growth

Received: June 24, 2025; **Revised:** August 2, 2025
Accepted: August 7, 2025

✉Address correspondence to linxzh8@mail.sysu.edu.cn

path of the absorber layer by introducing a NaOH-Se intermediate layer to obtain a highly crystalline film [13]. Wu et al. used an *in-situ* grown Na_2S passivation layer to suppress harmful decomposition reactions and reduce the formation of secondary phases [14]. Pack et al. grew a MoO_3 modification layer by thermal evaporation to adjust the interface energy-band alignment, significantly enhancing the carrier transport ability [15]. However, the above-mentioned back interface passivation layers could diffuse into the absorber layer during high-temperature selenization, bringing impurity in the bulk phase. Due to the excellent interfacial passivation capability and structural stability, SiO_2 passivation layers have been maturely applied in silicon solar cells [16]. Meanwhile, issues, such as high equipment costs, complex processes, strong thickness sensitivity, and poor large-area uniformity, still exist, making it difficult to achieve the simultaneous optimization of V_{OC} and FF.

Different from traditional passivation layers, the porous insulator contact (PIC) structure can form discrete local contact points at the interface by introducing porous insulator materials (such as porous alumina, porous silica, and porous silicon nitride) on the semiconductor surface or interface [17]. The concept of PIC draws on the local contact technology in silicon-based solar cells [18–21]. Carriers can be directly transported through the local opening areas of the porous insulator, without relying on the electron tunneling mechanism (which is sensitive to the dielectric thickness and affects the FF). This design expands the passivation area by increasing the interface coverage area of the porous insulator, thereby reducing the range of the recombination region and effectively suppressing carrier recombination, achieving the same passivation effect as traditional passivation layers [17].

In this work, we propose a novel back-interface engineering strategy for CZTSSe solar cells by replacing conventional porous insulators with solution-processed SiO_2 nanoparticle interlayers. The SiO_2 nanoparticles are deposited onto the molybdenum-coated glass substrates. Through a straightforward spin-coating deposition of SiO_2 nanoparticles onto molybdenum-coated glass substrates, we achieve dual improvements in crystalline quality and back-contact integrity. The synergistic mitigation of bulk and interface losses enables simultaneous optimization of V_{OC} and FF, ultimately yielding a power conversion efficiency of 10.72%—a 19% relative enhancement compared to the reference devices (9.03%). This interfacial modification strategy demonstrates the critical role of defect passivation and carrier transport optimization in overcoming efficiency limitations for solution-processed thin-film photovoltaics.

2 Results and discussion

2.1 Back interface processing based on SiO_2 nanoparticles

Figure 1(a) presents a schematic diagram of the CZTSSe solar cell structure featuring SiO_2 nanoparticle passivation at the back interface. The passivation treatment was applied via a solution process. Full fabrication details are provided in Section 4. To validate nanoparticle attachment to Mo-coated substrates, we performed scanning electron microscopy (SEM) on samples spin-coated with 4, 20, and 100 nm SiO_2 nanoparticles, alongside an untreated control (Figs. 1(b)–1(e)). Distinct nanoparticle coverage is evident on all SiO_2-treated Mo surfaces compared to the bare control, confirming the successful deposition of SiO_2 nanoparticles on the Mo surface. Notably, the 4 nm nanoparticle tends to gather together on the surface of substrate due to the high surface energy, whereas 20 and 100 nm particles remain well-dispersed (Figs. 1(c)–1(e)). The characteristic spherical morphology of SiO_2 nanoparticles is clearly resolved in the 20 and 100 nm samples.

2.2 Morphological and structural information of CZTSSe thin films

SEM was used to investigate the morphological effects of SiO_2 nanoparticles on CZTSSe thin films, and the results are shown in Figs. 2(a)–2(h). It is found that all films exhibit a bilayer structure composed of large grains on top and a thin fine grain layer at the bottom. The thickness of the films is approximately 620 nm, which is consistent with the definition of ultrathin CZTSSe solar cells (< 700 nm) [22]. Compared to the control, where pinholes can be observed, all samples coated with SiO_2 nanoparticles display a denser surface morphology with larger grains. The optimization of

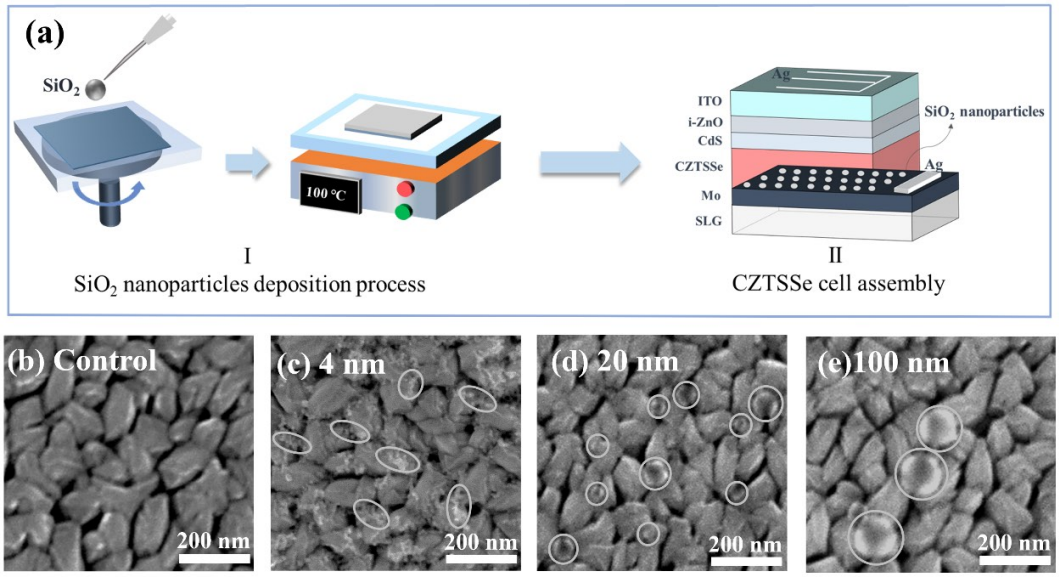

Figure 1 (a) Schematic diagram of the SiO_2 nanoparticle processing and the structure of CZTSSe solar cell with SiO_2 nanoparticles PIC structure. Top-view SEM images of the Mo surface of (b) control and covered with (c) 4 nm SiO_2 nanoparticles, (d) 20 nm SiO_2 nanoparticles, and (e) 100 nm SiO_2 nanoparticles.

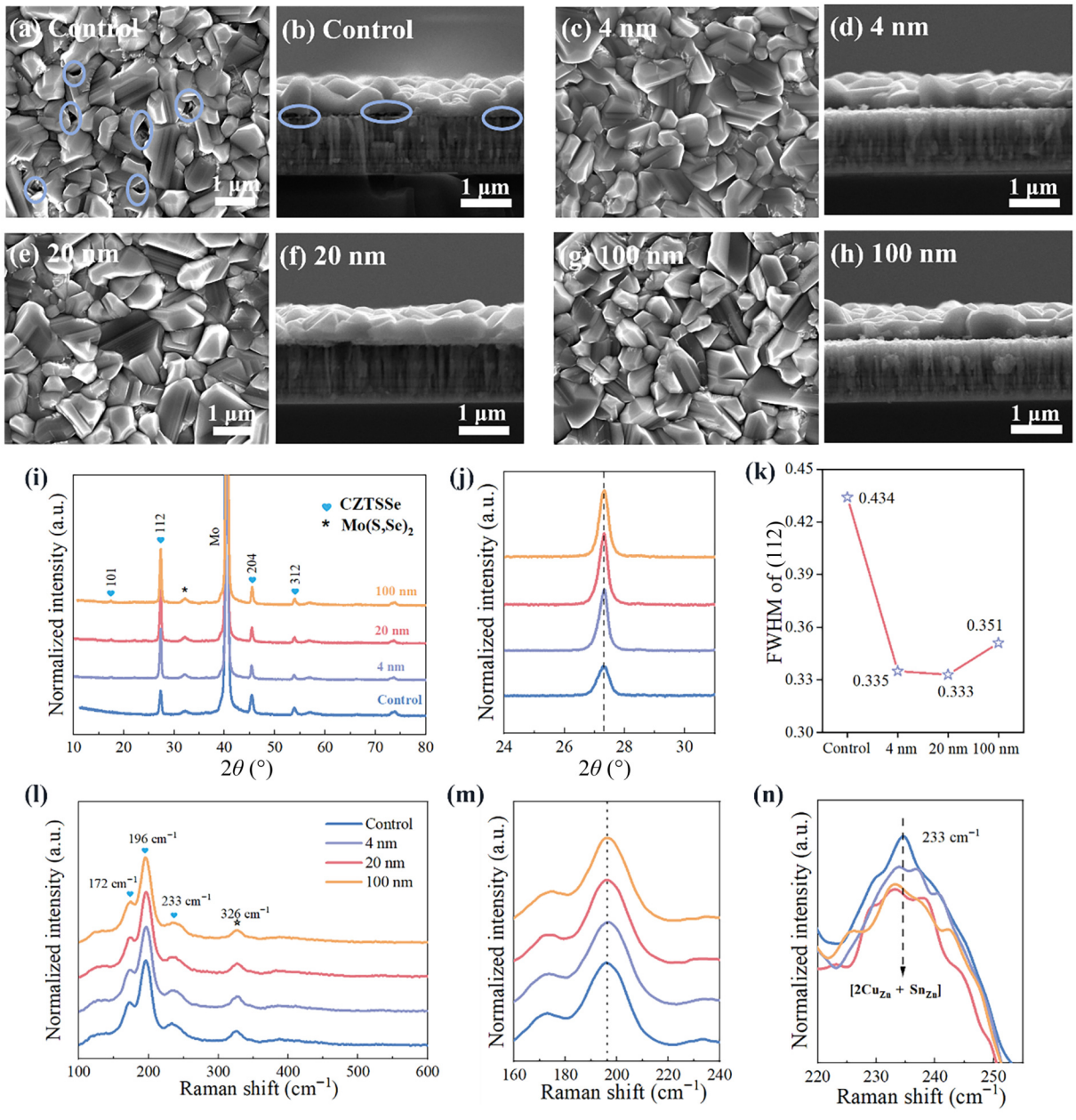

Figure 2 Top-view and cross-section SEM images of ((a) and (b)) control, ((c) and (d)) 4 nm, ((e) and (f)) 20 nm, and ((g) and (h)) 100 nm. (i) XRD patterns. (j) Magnified view of the (112). (k) FWHM of (112). (l) Raman spectra. (m) Magnified view of 196 cm^{-1}. (n) Magnified view of 233 cm^{-1}.

this crystallization improves the back-contact quality, which is conducive to the transport of holes to the back electrode. In addition, SiO_2 nanoparticles can hardly be observed via the cross-section SEM images (Figs. 2(d), 2(f), and 2(h)), likely due to their small size and complete coverage by the as-grown CZTSSe grains.

Then, X-ray diffraction (XRD) measurement was conducted to determine the phase structure of the CZTSSe films. As shown in Fig. 2(i), all samples displayed similar diffraction peaks. The characteristic diffraction peaks belonging to (101), (112), and (204) lattice planes of kesterite CZTSSe are detected [23], indicating the formation of kesterite CZTSSe. The (112) main peak position of all samples coated with SiO_2 nanoparticles shows no shift compared with that of the control, indicating that the Si from SiO_2 nanoparticles does not enter the CZTSSe lattice (Fig. 2(j)). Additionally, 4, 20, and 100 nm films exhibit a narrower full width at half maximum (FWHM) than that of SiO_2-0 film (Fig. 2(k)), suggesting that the CZTSSe thin film with SiO_2 nanoparticles coated at the back interface exhibits better crystallinity [24].

To further confirm the phase purity of the CZTSSe films, Raman spectroscopy was carried out. As shown in Fig. 2(l), the Raman peaks appearing at 172, 196, and 233 cm^{-1} can be attributed to the B mode, A mode, and E mode of CZTSSe, respectively, while the peak at 326 cm^{-1} corresponds to Cu_2ZnSnS_4 (CZTS) [25, 26]. Meanwhile, the Raman spectra reveal no detectable secondary phases, such as $Cu_2S(Se)$ and ZnS(Se). In brief, the introduction of SiO_2 nanoparticles has no effect on the phase purity of CZTSSe films. The main Raman band of all samples is located at the same position of 196 cm^{-1}, further implying that Si from SiO_2 nanoparticles is not doped into the CZTSSe lattice (Fig. 2(m)). Additionally, the Raman peak intensity at 233 cm^{-1} serves as an

indicator of the [$2Cu_{Zn}$ + Sn_{Zn}] defect cluster concentration in CZTSSe films, where higher peak intensity corresponds to greater defect density [27]. It is found that the [$2Cu_{Zn}$ + Sn_{Zn}] defect cluster concentration in the films coated with SiO_2 nanoparticles is significantly lower (Fig. 2(n)) with the 20 and 100 nm samples reaching the minimum. The lower defect cluster concentration in 20 and 100 nm samples compared to that of 4 nm sample could be related to the reduction of agglomeration distribution issue of SiO_2 nanoparticles.

2.3 Electrical property of CZTSSe films

Conductive atomic force microscopy (C-AFM) was employed to study the surface roughness and conductivity of CZTSSe thin films [28]. As shown in Fig. 3, the grain boundaries (GBs) of all films exhibit a brighter contrast than intra-grain (IGs), indicating a better current transport capability at GBs. The average current and root-mean-square roughness (R_q) based on C-AFM are summarized in Table 1. It is found that the average current of all samples coated with SiO_2 nanoparticles is higher than that of the control (only 0.224 pA), denoting that the introduction of SiO_2 nanoparticles can suppress the carrier recombination. This enhancement of carrier transport capability at GBs of the film is favorable to promote the spatial separation of carriers and thus reduce carrier recombination [29]. Additionally, the R_q of 4, 20, and 100 nm films (78, 71, and

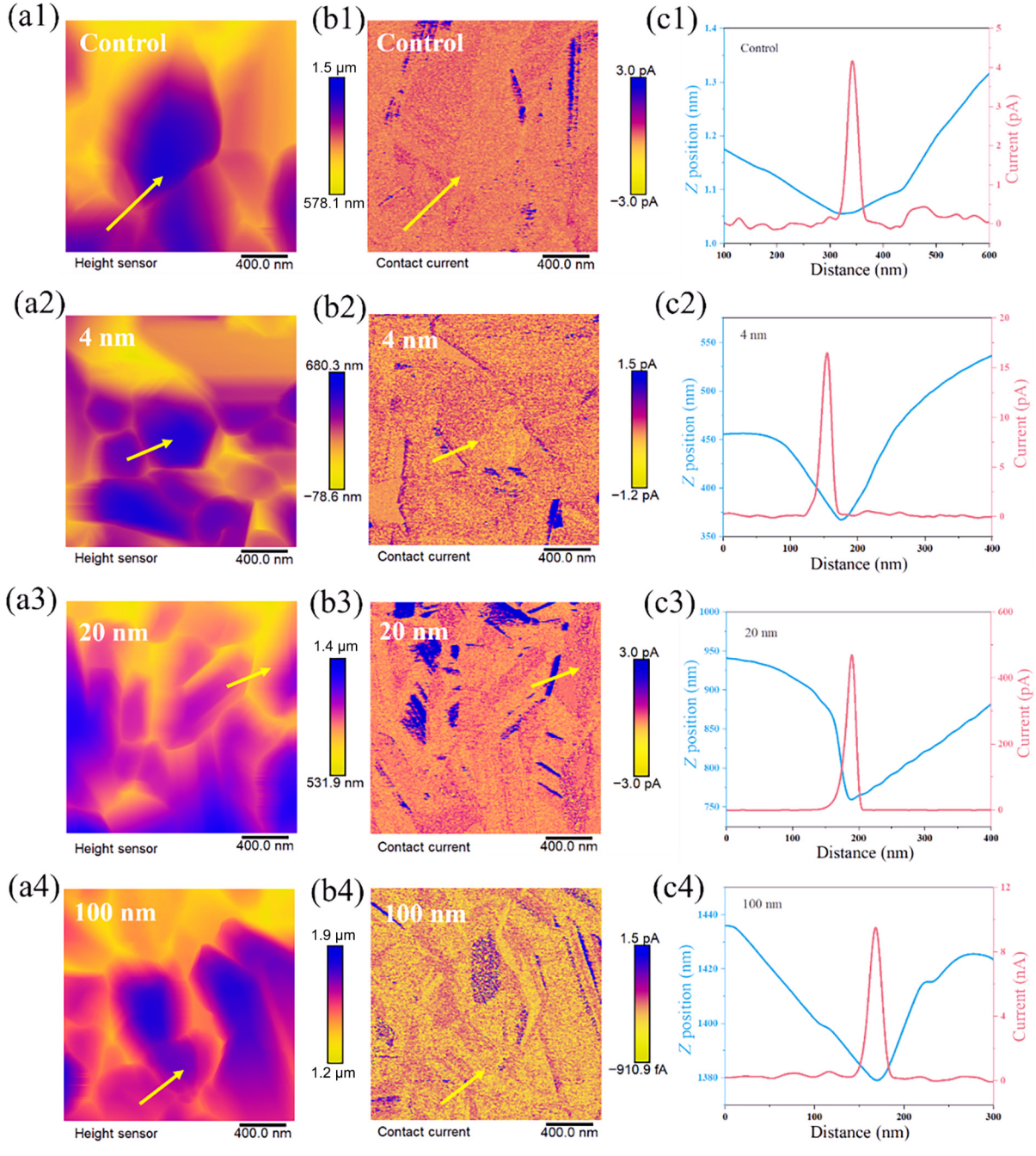

Figure 3 (a1)–(a4) AFM images of control, 4, 20, and 100 nm samples. (b1)–(b4) The corresponding C-AFM images. (c1)–(c4) Surface current and height images along the yellow arrows.

Table 1 Roughness and average current of SiO_2-0 and SiO_2-20 nm films. R_a stands for arithmetic average roughness

Sample	R_a (nm)	R_q (nm)	Average current (pA)
Control	128	102	0.224
4 nm	97	78	0.499
20 nm	91	71	2.65
100 nm	101	83	0.676

83 nm, respectively) is significantly lower than the control (102 nm), which is consistent with SEM results. The smoother surface is expected to form better contact with the CdS layer, inhibiting carrier recombination at the front interface and thus improving device performance [30]. In brief, the introduction of SiO_2 nanoparticles at the back interface can enhance the electrical conductivity of the CZTSSe thin film and result in a smoother and denser film.

2.4 Performance of CZTSSe solar cells

To estimate the influence of SiO_2 nanoparticles on the performance of CZTSSe thin film solar cells, current density–voltage (*J–V*) characterization was performed. Figures 4(a)–4(d) show the statistical data of PCE, V_{OC}, current density (J_{SC}), and FF of control, 4, 20, and 100 nm devices. Obviously, the PCE is dramatically enhanced with the insertion of SiO_2 nanoparticles due to the improvement of V_{OC} and FF, which reaches maximum when the size of the SiO_2 nanoparticle is raised to 20 nm. The *J–V* curves of the champion devices are shown in Fig. 4(e), with detailed photovoltaic parameters being summarized in Table 2. The PCE increases from 9.03% to 10.72% when applying 20 SiO_2 nanoparticles PIC passivation structure, which is attributed to the significant enhancement in both V_{OC} (from 0.458 to 0.495 V) and FF (from 63.5% to 67.1%). This improvement in V_{OC} and FF mainly results from the introduction of SiO_2 nanoparticles at the CZTSSe back interface, which enhances the crystal quality and passivates the deep defects at back interface.

Figure 4(f) depicts the passivation mechanism of SiO_2 nanoparticles. The nanoparticles are dispersed on Mo substrate, forming a PIC structure at the CZTSSe back interface. When holes are transported towards the back electrode, they will be blocked by the insulating SiO_2 nanoparticles and can only pass through the gaps between the particles (hole transport path 2). According to the theoretical equation of the semiconductor surface recombination [31, 32]

$$S_P = \sigma_+ v_t N_{st} \quad (1)$$

where S_p is the hole surface recombination rate, σ_+ is the interface state capture cross-section, v_t is the carrier thermal motion velocity, and N_{st} is the interface state density per unit area. It can be known that when S_p remains unchanged, the larger the total interface contact area (S) is, the greater the interface total recombination will be ($R = SS_p$). In brief, the PIC structure based on insulating SiO_2

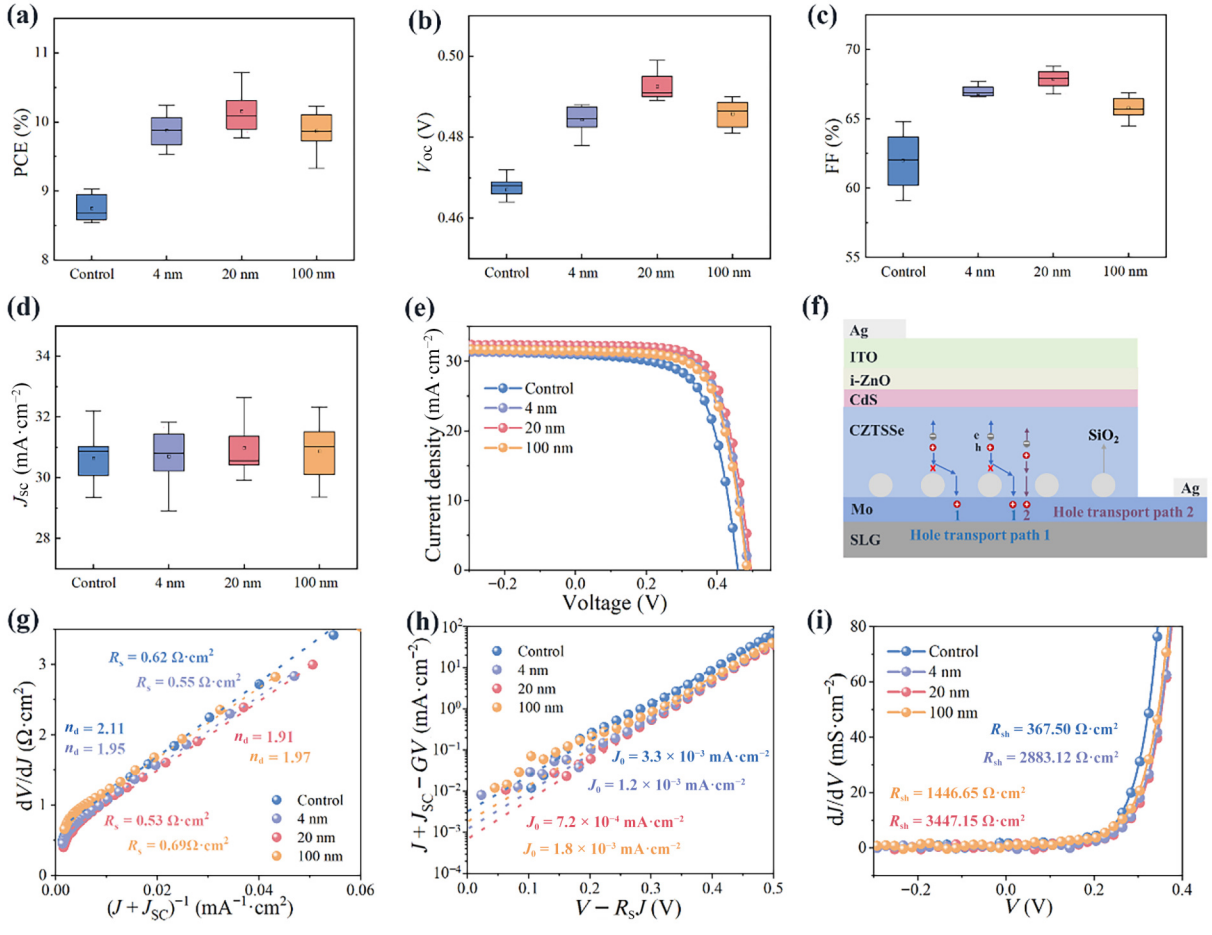

Figure 4 ((a)–(d)) Statistical box plots based on 36 devices for the PCE, V_{OC}, J_{SC}, and FF of control, 4, 20, and 100 nm devices. (e) *J–V* curves. (f) Diagram of passivation mechanism with SiO_2 nanoparticles. (g) d*J*/d*V* versus $(J+J_{SC})^{-1}$ curves. (h) $J+J_{SC}-GV$ (*G* stands for shunt conductance) versus $V-R_sJ$ curves. (i) d*J*/d*V* versus *V* curves.

Table 2 Performance parameters for the champion device of control, 4, 20, and 100 nm samples

Device	PCE (%)	V_{OC} (V)	J_{SC} (mA·cm^{-2})	FF (%)	R_{sh} (Ω·cm^2)	R_s (Ω·cm^2)	n_d	J_0 (mA·cm^{-2})
Control	9.03	0.458	31.03	63.5	367.50	0.62	2.11	3.3×10^{-3}
4 nm	10.34	0.488	31.66	66.8	2883.12	0.55	1.95	1.2×10^{-3}
20 nm	10.72	0.495	32.29	67.1	3447.15	0.53	1.91	7.2×10^{-4}
100 nm	10.11	0.490	31.50	65.4	1446.15	0.69	1.97	1.8×10^{-3}

nanoparticles directly reduces the total interface contact area at the CZTSSe/Mo interface, thus reducing the total interface recombination. This is beneficial to reducing non-radiative recombination at the back interface, thus improving the photovoltaic parameters of the device. Meanwhile, the size of SiO_2 nanoparticle will affect the PIC passivation structure. As shown in Figs. 1(c)–1(e), 4 nm SiO_2 nanoparticles are prone to agglomeration, while 100 nm SiO_2 nanoparticles would prolong the hole transport path (hole transport path 2).

To further understand the effect of SiO_2 nanoparticles on device performance, the single exponential diode equation was used to extract key diode parameters of solar cells [33]

$$J = J_0 \exp\left(\frac{q}{n_d kT}(V - R_s J)\right) + G_{sh} V - J_L \quad (2)$$

$$r(J) = \frac{dV}{dJ} = R_s + \frac{n_d kT}{q}(J + J_L)^{-1} \quad (3)$$

where $r(J)$ is dV/dJ, J_0 represents the reverse saturation current density, q refers to elementary charge, R_s is the series resistance, G_{sh} is the shunt conductance, T is the absolute temperature, k is the Boltzmann constant, J_L is the photocurrent density, and n_d is the ideality factor associated with recombination behavior. The fitting results of key diode parameters are presented in Figs. 4(g)–4(i). As shown in Fig. 4(g), the ideality factors (n_d) are calculated to be 2.11, 1.95, 1.91, and 1.97, respectively, for the control, 4, 20, and 100 nm devices (Fig. 4(g)) [34]. The consistently lower n_d values in SiO_2-coated devices indicate improved p–n junction quality, contributing to enhanced device performance [35, 36].

Figure 4(h) reveals that the J_0 is significantly reduced in SiO_2-modified devices compared to the control, further confirming suppressed interface charge recombination due to nanoparticle incorporation [37]. Furthermore, the shunt resistance (R_{sh}) increases substantially with SiO_2 addition (Fig. 4(i)), reaching a maximum of 3447.15 Ω·cm^2 for the 20 nm device. In contrast, the R_s varies minimally across all devices, with the lowest value observed for the 20 nm sample (Fig. 4(g)).

Collectively, the optimized diode parameters (n_d, J_0, and R_{sh}) achieved through SiO_2 back-interface modification directly contribute to the enhanced V_{OC} and FF [38]. Among the variants, the 20 nm device exhibits optimal parameters. This superiority likely stems from its ideal localized contact structure: The 4 nm nanoparticles are prone to agglomeration, compromising uniformity, while the 100 nm particles increase hole transport path length, reducing effectiveness.

The external quantum efficiency (EQE) measurement was performed to further reveal the underlying mechanism of the enhanced cell performance [39]. As shown in Fig. 5(a), the EQE curves of the control, 4, 20, and 100 nm devices overlap substantially, indicating that SiO_2 nanoparticles do not affect the light-harvesting capability of the devices. The integrated current densities derived from the EQE spectra are 30.64, 30.56, 31.35, and 31.06 mA·cm^{-2}, respectively, which are all less than 4% difference

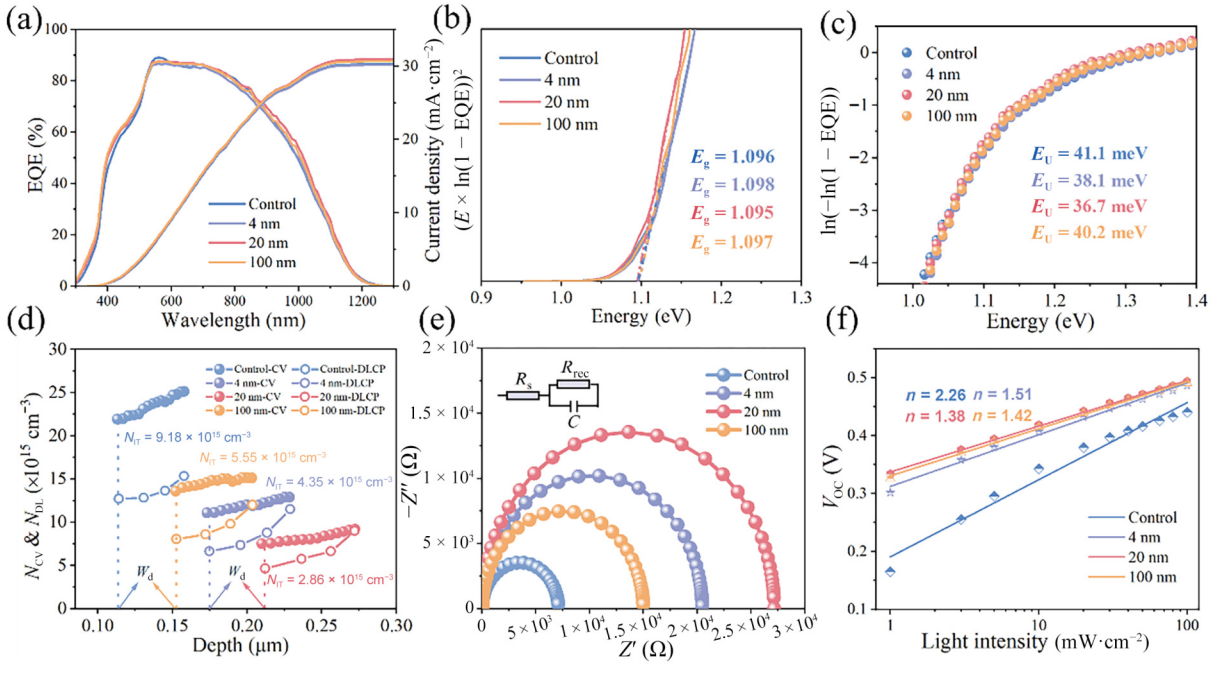

Figure 5 (a) EQE curves of the control, 4, 20, and 100 nm optimal devices. (b) Bandgaps estimated from EQE. (c) Urbach energy of absorption layers estimated from EQE. (d) *C*–*V* and DLCP profiles. (e) EIS spectra. (f) Light intensity dependent of V_{OC}.

compared with the corresponding value obtained from *J*–*V* analysis. The optical bandgaps (E_g) calculated from the EQE spectra are 1.096, 1.098, 1.095, and 1.097 eV for control, 4, 20, and 100 nm samples, respectively (Fig. 5(b)), which is nearly unchanged. This is consistent with the XRD and Raman results. To further evaluate the influence of SiO_2 nanoparticles on the band tail states, the Urbach energy (E_U) of the absorber layers was further calculated based on the EQE spectra. As shown in Fig. 5(c), the E_U is 41.1, 38.1, 36.7, and 40.2 meV for control, 4, 20, and 100 nm samples, respectively. The decrease of samples coated with SiO_2 nanoparticles in E_U suggests that the introduction of SiO_2 nanoparticles at the back interface can effectively suppress the band tail states, which is beneficial for increasing the V_{OC}, thus improving device performance [40, 41].

To understand the defect and interface recombination properties, capacitance–*V* (*C*–*V*) and drive level capacitance profile (DLCP) measurements are conducted, and the results are presented in Fig. 5(d) [42]. Generally, the *C*–*V* measurement is sensitive to both bulk defects and interface defects, while the DLCP measurement is only sensitive to bulk defects [43]. Thus, the difference between them at zero bias represents the interface defect density (N_{IT}) in the device. The defect density and depletion region width (W_d) derived from the DLCP and *C*–*V* data are listed in Table 3, which can be calculated by the following equations [44, 45]

$$N_{CV} = \frac{C^3}{qA^2\varepsilon_r\varepsilon_0}\left(\frac{dC}{dV}\right)^{-1} \quad (4)$$

$$N_{DL} = \frac{C_0^{\ 3}}{2qA^2\varepsilon_r\varepsilon_0 C_1} \quad (5)$$

$$W_d = \frac{\varepsilon_r\varepsilon_0 A}{C} \quad (6)$$

where the N_{CV} and N_{DL} are carrier concentration derived from C–V and DLCP measurement. C_1 and C_0 are the test capacitance and small molecule capacitance, respectively. ε_0 and ε_r refer to the vacuum dielectric constant and the relative dielectric constant, respectively, and *A* represents the total area of the solar cell. The results show that the N_{IT} values of the 20 nm sample (2.86×10^{15} cm^{-3}) are the lowest, indicating optimal local contact passivation structure for 20 nm SiO_2 nanoparticles sample. The lower density of interface defect is helpful to suppress the interface recombination, contributing to a higher V_{OC}. In addition, the W_d of the devices increased obviously after the introduction of SiO_2, which is beneficial for carrier separation and can also suppress recombination.

Electrochemical impedance spectroscopy (EIS) is employed to further evaluate interface impact of SiO_2 nanoparticles on interface recombination of CZTSSe solar cells [46]. As shown in Fig. 5(e), the device with 20 nm SiO_2 nanoparticles exhibits the largest recombination resistance (R_{rec}) (R_{rec} = 27.4 kΩ), significantly surpassing that of the control device (7.1 kΩ). Since a larger value of R_{rec} corresponds to a lower interface recombination [47], these results confirm that SiO_2 nanoparticles provide effective passivation at the interface.

Furthermore, the dependence of V_{OC} on light intensity provides additional insight into interface carrier recombination of the CZTSSe solar cell [48]. As shown in Fig. 5(f), by fitting the curves, the slope values of the control (2.26), 4 nm (1.51), 20 nm (1.38), and 100 nm (1.42) devices are estimated, which correspond to the ideality factors (*n*) related to carrier recombination. The lower *n* values of in SiO_2-modified devices indicate effective suppression of Shockley–Read–Hall (SRH) recombination in the device [49], which is consistent with the EIS analysis. Collectively, these findings demonstrate that SiO_2 nanoparticle passivation at the CZTSSe/Mo back interface mitigates carrier recombination, directly contributing to the enhanced device performance.

3 Conclusions

In summary, we developed a simple strategy to suppress severe back-interface carrier recombination in CZTSSe solar cells by incorporating SiO_2 nanoparticle at the Mo/CZTSSe interface. This approach creates a discrete local contact structure, leveraging the insulating properties of SiO_2 to enhance absorber crystallinity, reduce interfacial defect density, and specifically suppress detrimental [$2Cu_{Zn}$ + Sn_{Zn}] deep-level clusters. Critically, by reducing the back-interface recombination area and lowering interfacial defect density, this localized passivation mechanism significantly suppresses carrier recombination, leading to substantial gains in V_{OC} and FF. Consequently, the power conversion efficiency of ultrathin CZTSSe devices increased from 9.03% to 10.72%. This work presents a novel and effective method for enhancing back-contact quality and overcoming efficiency bottlenecks in CZTSSe photovoltaics.

4 Experimental section

4.1 Materials and reagents

$Cu(NO_3)_2{\cdot}3H_2O$ (99.99%), $Zn(CH_3COO)_2$ (99.99%), $SnCl_2{\cdot}2H_2O$ (99.9%), dimethyl sulfoxide (DMSO, 99.9%), and N,N-dimethylformamide (DMF, 99.9%) were purchased from Macklin. $AgNO_3$ (99.8%) and $CdSO_4{\cdot}8/3H_2O$ (99.99%) were purchased from Aladdin. Thiourea (Tu, 99%) and ammonia solution (25%–28%) were purchased from Alfa. The SiO_2 nanoparticles dispersion was purchased from Thermo Fisher Scientific. SLG-Mo substrate was purchased from Suzhou Shangyang Solar Energy Technology Co, Ltd., model Mo-20E-23. Selenium particles (99.999%) were purchased from Zhong Nuo Advanced Material. All the chemicals were used directly without further purification.

Table 3 The device characteristics of the control, 4, 20, and 100 nm devices derived from EQE, *C*–*V*, DLCP, EIS, and light intensity dependent

Sample	E_g (eV)	E_U (meV)	N_{CV} (cm^{-3})	N_{DL} (cm^{-3})	N_{IT} (cm^{-3})	W_d (μm)	R_{rec} (kΩ)	*n*
Control	1.096	41.1	2.51×10^{16}	1.27×10^{16}	9.18×10^{15}	0.114	7.1	2.26
4 nm	1.098	38.1	1.10×10^{16}	6.65×10^{15}	4.35×10^{15}	0.174	20.5	1.51
20 nm	1.095	36.7	7.50×10^{15}	4.64×10^{15}	2.86×10^{15}	0.212	27.4	1.38
100 nm	1.097	40.2	1.36×10^{16}	8.05×10^{15}	5.55×10^{15}	0.152	15.0	1.42

4.2 Back interface processing based on SiO_2 nanoparticles

The back interface treatment was performed using a solution method: First, the purchased aqueous dispersion of SiO_2 nanoparticles was diluted with deionized water to obtain solutions with different nanoparticle sizes (4, 20, and 100 nm), and the mass concentrations of all dispersions were maintained at 0.30 wt.%. Then, the diluted aqueous dispersion was directly dropped onto the molybdenum-coated substrate that had been plasma-cleaned for 4 min, followed by spin-coating. Finally, the substrate was heated at 100 °C for 2 min to complete the treatment process.

4.3 Fabrication of CZTSSe solar cells

4.3.1 Preparation of the absorber layers

First, the Cu-Zn-Sn-S precursor inks were prepared by dissolving $AgNO_3$ (99.5%), $Cu(NO_3)_2{\cdot}3H_2O$ (99.99%), $C_6H_5Na_3O_7{\cdot}2H_2O$ (99.7%), $SnCl_2{\cdot}2H_2O$, $Zn(CH_3COO)_2$ (99.99%), and Tu (99%) into DMSO and DMF mixed solution, stirred at 25 °C to obtain a light yellow precursor solution. The molar ratios of (Ag + Cu)/(Zn + Sn), Zn/Sn, and Ag/(Ag + Cu) were 0.66, 1.5, and 0.03, respectively. The concentrations of metal elements and thiourea were 1.82 and 2.66 $mol{\cdot}L^{-1}$, respectively. Then, the prepared solution was spun at 2000 rpm for 60 s. Mo substrate was pre-coated with SiO_2 nanoparticles, followed by heating at 320 °C for 2 min. The above coating and drying processes were carried out 4 times to obtain the CZTS precursor film. Finally, the precursor film was selenized under Se and S atmosphere with a S/Se mass ratio of 1.4% (300 s at 400 °C, followed by 840 s at 540 °C) to form the CZTSSe absorber with thickness of approximately 600 nm.

4.3.2 Device fabrication

First, the CdS buffer layer of 50 nm was prepared by the chemical bath deposition (CBD). Subsequently, intrinsic zinc oxide (i-ZnO) and indium tin oxide (ITO) layers (50 and 200 nm, respectively) were sputtered on the CdS layer by magnetron sputtering device. Finally, Ag electrodes were deposited by vacuum thermal evaporation to form top contact. In this work, the MgF_2 antireflection layers were not used, and the full area of each device was 0.6 cm × 0.6 cm.

4.4 Characterizations

The micromorphology of the CZTSSe thin film was recorded via a field emission SEM (FE-SEM; HITACHI Regulus 8230). The structure information was characterized via XRD (D-MAX 2200 VPC with an operating voltage of 40 kV and a current density of 40 mA) and Raman spectroscopy (Renishaw in Via Reflex) with an excitation wavelength of 633 nm. The atomic force microscope (AFM) and C-AFM (Dimension Icon, Bruker) were used to investigate the surface roughness and potential distribution of CZTSSe films. *J*–*V* curves were measured under AM 1.5 G illumination (VS-6821 M solar simulator), which was calibrated with a monocrystalline Si reference cell. External quantum efficiency (EQE) was measured using a QE-R instrument from Enlitech in the range of 300 to 1300 nm, which was calibrated with Si and Ge reference diodes. *C*–*V* and drive-level capacitance profiling (DLCP) were performed in the dark using the semiconductor characterization test system (Keithley 4200A-SCS). The *C*–*V* measurements were conducted at a frequency of 100 kHz with a direct current (DC) bias voltage sweeping from −1.0 to 0.8 V, and the DLCP measurements were performed at a frequency of 100 kHz with the alternating current (AC) amplitude varying from 15 to 135 mV. EIS was performed using the Zahner Zennium electrochemical workstation.

Data availability

All data needed to support the conclusions in the paper are presented in the manuscript and the Electronic Supplementary Material. Additional data related to this paper may be requested from the corresponding author upon request.

Acknowledgements

The authors acknowledge the financial support from the National Natural Science Foundation of China (No. 62074168), the Guangdong Basic and Applied Basic Research Foundation (No. 2024A1515140104), and the funding from the State Key Laboratory of Optoelectronic Materials and Technologies at Sun Yat-Sen University (No. OEMT-2022-ZTS-08). The authors also thank Prof. Zongcun Liang, Prof. Ruijiang Hong, Prof. Bin Ai, Prof. Fei Guo, and Prof. Yi Fang for the facility and characterization support.

Declaration of competing interest

All the contributing authors report no conflict of interests in this work.

Author contribution statement

X. Z. L. supervised the project at the Sun Yat-Sen University of China. Y. Y. H. and X. Z. L. conceived the original concept and designed the experiments. Y. Y. H. fabricated the devices and conducted the photovoltaic characterization and analysis. Y. Y. H., Y. M., and Y. M. D. conducted the SEM specimen preparation, the EQE characterization and performed the characterization and analysis. W. J. C. and Z. Y. R. performed the CV measurements. Y. Y. H., Y. M., Y. M. D., M. Y. W., E. N. G., and X. Z. L. contributed to the discussion and further evaluation of the data. Y. Y. H., E. N. G., G. W. Y., and X. Z. L. drafted the manuscript. All the coauthors contributed to reviewing and revising the manuscript. All the authors have approved the final manuscript.

Use of AI statement

None.

References

[1] Ji, Y. X.; Zhao, X. Y.; Pan, Y. N.; Su, Z. H.; Lin, J. H.; Akinoglu, E. M.; Xu, Y.; Zhang, H. Y.; Zhao, P. J.; Dong, Y. et al. CuSCN modified back contacts for high performance CZTSSe solar cells. *Adv. Funct. Mater.* **2023**, *33*, 2211421.

[2] Antunez, P. D.; Bishop, D. M.; Lee, Y. S.; Gokmen, T.; Gunawan, O.; Gershon, T. S.; Todorov, T. K.; Singh, S.; Haight, R. Back contact engineering for increased performance in kesterite solar cells. *Adv. Energy Mater.* **2017**, *7*, 1602585.

[3] Todorov, T. K.; Reuter, K. B.; Mitzi, D. B. High-efficiency solar cell with earth-abundant liquid-processed absorber. *Adv. Mater.* **2010**, *22*, E156–E159.

[4] Li, J. J.; Huang, J. L.; Cong, J. L.; Mai, Y.; Su, Z. H.; Liang, G. X.; Wang, A.; He, M. R.; Yuan, X. J.; Sun, H. et al. Large-grain spanning monolayer $Cu_2ZnSnSe_4$ thin-film solar cells grown from metal precursor. *Small* **2022**, *18*, 2105044.

[5] Li, Y. M.; Cui, C. C.; Wei, H.; Shao, Z. P.; Wu, Z. C.; Zhang, S.; Wang, X.; Pang, S. P.; Cui, G. L. Suppressing element inhomogeneity enables 14.9% efficiency cztsse solar cells. *Adv. Mater.* **2024**, *36*, 2400138.

[6] Green, M. A.; Dunlop, E. D.; Yoshita, M.; Kopidakis, N.; Bothe, K.; Siefer, G.; Hinken, D.; Rauer, M.; Hohl-Ebinger, J.; Hao, X. J. Solar cell efficiency tables (Version 64). *Prog. Photovolt.* **2024**, *32*, 425–441.

[7] Liu, F. Y.; Wu, S. X.; Zhang, Y.; Hao, X. J.; Ding, L. M. Advances in kesterite $Cu_2ZnSn(S,Se)_4$ solar cells. *Sci. Bull.* **2020**, *65*, 698–701.

[8] Li, Y. M.; Wei, H.; Cui, C. C.; Wang, X.; Shao, Z. P.; Pang, S. P.; Cui, G. L. CZTSSe solar cells: Insights into interface engineering. *J. Mater. Chem. A* **2023**, *11*, 4836–4849.

[9] Guc, M.; Gurieva, G.; Hajdeu-Chicarosh, E.; Schorr, S.; Lisunov, K. G.; Arushanov, E. Conductivity mechanisms and influence of the Cu/Zn disorder on electronic properties of the powder $Cu_2ZnSn(S_{1-x}Se_x)_4$ solid solutions. *J. Mater. Res. Technol.* **2021**, *13*, 2251–2259.

[10] Kim, S. Y.; Son, D. H.; Kim, Y. I.; Kim, S. H.; Kim, S.; Ahn, K.; Sung, S. J.; Hwang, D. K.; Yang, K. J.; Kang, J. K. et al. Void and secondary phase formation mechanisms of CZTSSe using Sn/Cu/Zn/Mo stacked elemental precursors. *Nano Energy* **2019**, *59*, 399–411.

[11] Scragg, J. J.; Kubart, T.; Wätjen, J. T.; Ericson, T.; Linnarsson, M. K.; Platzer-Björkman, C. Effects of back contact instability on Cu_2ZnSnS_4 devices and processes. *Chem. Mater.* **2013**, *25*, 3162–3171.

[12] Kim, S. Y.; Hong, S.; Kim, S. H.; Son, D. H.; Kim, Y. I.; Kim, S.; Heo, Y. W.; Kang, J. K.; Kim, D. H. Effect of Al_2O_3 dot patterning on cztsse solar cell characteristics. *Nanomaterials* **2020**, *10*, 1874.

[13] Li, Y. F.; Jian, Y.; Huang, F.; Zhou, N.; Chai, W. Q.; Hu, J. G.; Zhao, J.; Su, Z. H.; Chen, S.; Liang, G. X. Suppressing deep-level trap toward over 13% efficient solution-processed kesterite solar cell. *Small* **2024**, *20*, 2401330.

[14] Jian, Y.; Xie, T. L.; Han, L. T.; Kou, D. X.; Zhou, W. H.; Zhou, Z. J.; Yuan, S. J.; Meng, Y. N.; Qi, Y. F.; Wu, S. X. Modification of back interfacial contact with MoO_3 layer *in situ* introduced by Na_2S aqueous solution for efficient kesterite CZTSSe solar cells. *J. Mater. Chem. C* **2023**, *11*, 4634–4644.

[15] Park, J.; Huang, J. L.; Sun, K. W.; Ouyang, Z.; Liu, F. Y.; Yan, C.; Sun, H.; Pu, A. B.; Green, M.; Hao, X. J. The effect of thermal evaporated MoO_3 intermediate layer as primary back contact for kesterite Cu_2ZnSnS_4 solar cells. *Thin Solid Films* **2018**, *648*, 39–45.

[16] Qiu, J. W.; Zhou, Z. G.; Zhang, L. J.; Song, X. M.; Zhong, S. H.; Yin, H. P.; Tong, R.; Zhang, J. H.; Shen, W. Z.; Huang, Z. G. Pinhole-like carriers transport in spin-coating SiO_2 enabling high-efficiency dopant-free Si solar cells. *Chem. Eng. J.* **2024**, *495*, 153672.

[17] Peng, W.; Mao, K. T.; Cai, F. C.; Meng, H. G.; Zhu, Z. J.; Li, T. Q.; Yuan, S. J.; Xu, Z. J.; Feng, X. Y.; Xu, J. H. et al. Reducing nonradiative recombination in perovskite solar cells with a porous insulator contact. *Science* **2023**, *379*, 683–690.

[18] Allen, T. G.; Bullock, J.; Yang, X. B.; Javey, A.; De Wolf, S. Passivating contacts for crystalline silicon solar cells. *Nat. Energy* **2019**, *4*, 914–928.

[19] Feldmann, F.; Bivour, M.; Reichel, C.; Hermle, M.; Glunz, S. W. Passivated rear contacts for high-efficiency n-type Si solar cells providing high interface passivation quality and excellent transport characteristics. *Sol. Energy Mater. Sol. Cells* **2014**, *120*, 270–274.

[20] Franklin, E.; Fong, K.; McIntosh, K.; Fell, A.; Blakers, A.; Kho, T.; Walter, D.; Wang, D.; Zin, N.; Stocks, M. et al. Design, fabrication and characterisation of a 24.4% efficient interdigitated back contact solar cell. *Prog. Photovolt.* **2016**, *24*, 411–427.

[21] Green, M. A. The path to 25% silicon solar cell efficiency: History of silicon cell evolution. *Prog. Photovolt.* **2009**, *17*, 183–189.

[22] Platzer Björkman, C.; Larsen, J. K.; Saini, N.; Babucci, M.; Martin, N. Ultrathin wide band gap kesterites. *Faraday Discuss.* **2022**, *239*, 38–50.

[23] Guo, J. Y.; Wang, L.; SiQin, L.; Yang, C. J.; Wang, Y. T.; Wang, Y. M.; Li, S. Y.; Liu, R. J.; Zhu, C. J.; Luan, H. M. CdS(In)/CZTSSe bandgap alignment engineering for performance enhancement of solar cells without ZnO layer. *Sol. Energy Mater. Sol. Cells* **2024**, *269*, 112787.

[24] Liang, G. X.; Li, Z. D.; Ishaq, M.; Zheng, Z. H.; Su, Z. H.; Ma, H. L.; Zhang, X. H.; Fan, P.; Chen, S. Charge separation enhancement enables record photocurrent density in $Cu_2ZnSn(S,Se)_4$ photocathodes for efficient solar hydrogen production. *Adv. Energy Mater.* **2023**, *13*, 2300215.

[25] Xu, H.; Ge, S. J.; Yang, W. T.; Khan, S. N.; Huang, Y. X.; Mai, Y. H.; Gu, E. N.; Lin, X. Z.; Yang, G. W. 9.63% efficient flexible $Cu_2ZnSn(S,Se)_4$ solar cells fabricated via scalable doctor-blading under ambient conditions. *J. Mater. Chem. A* **2021**, *9*, 25062–25072.

[26] Grossberg, M.; Krustok, J.; Raudoja, J.; Timmo, K.; Altosaar, M.; Raadik, T. Photoluminescence and Raman study of $Cu_2ZnSn(Se_xS_{1-x})_4$ monograins for photovoltaic applications. *Thin Solid Films* **2011**, *519*, 7403–7406.

[27] Li, J. J.; Huang, Y. C.; Huang, J. L.; Liang, G. X.; Zhang, Y. X.; Rey, G.; Guo, F.; Su, Z. H.; Zhu, H. B.; Cai, L. L. et al. Defect control for 12.5% efficiency $Cu_2ZnSnSe_4$ kesterite thin-film solar cells by engineering of local chemical environment. *Adv. Mater.* **2020**, *32*, 2005268.

[28] Li, J. B.; Chawla, V.; Clemens, B. M. Investigating the role of grain boundaries in CZTS and CZTSSe thin film solar cells with scanning probe microscopy. *Adv. Mater.* **2012**, *24*, 720–723.

[29] Yang, C. J.; Siqin, L.; Wang, Y. T.; Li, Y. F.; Li, W. B.; Li, S. Y.; Liu, R. J.; Luan, H. M.; Zhu, C. J. SnS-induced element diffusion Simultaneous optimization of interface and bulk defects in high-efficiency CZTSSe solar cells. *Chem. Eng. J.* **2025**, *503*, 158283.

[30] Jian, Y.; Han, L. T.; Kong, X. R.; Xie, T. L.; Kou, D. X.; Zhou, W. H.; Zhou, Z. J.; Yuan, S. J.; Meng, Y. N.; Qi, Y. F. et al. Segmented control of selenization environment for high-quality $Cu_2ZnSn(S,Se)_4$ films toward efficient kesterite solar cells. *Small* **2024**, *8*, 2400041.

[31] Yang, Y. H.; Cheng, S. Y.; Zhu, X. L.; Li, S.; Zheng, Z.; Zhao, K.; Ji, L. W.; Li, R. M.; Liu, Y.; Liu, C. et al. Inverted perovskite solar cells with over 2000 h operational stability at 85 °C sing fixed charge passivation. *Nature Energy* **2024**, *9*, 37–46.

[32] Guo, Y. X.; Yao, F.; Zhang, Y. C.; Chen, G. Y.; Du, S. J.; Yu, Z. X.; Zhou, H.; Ke, W. J.; Li, C.; Fang, G. J. A universal surface fixed charge reconstruction strategy to minimize contact loss in wide bandgap perovskite photovoltaics. *Energy Environ. Sci.* **2025**, *18*, 4916–4924.

[33] Hegedus, S. S.; Shafarman, W. N. Thin-film solar cells: Device measurements and analysis. *Prog. Photovolt.* **2004**, *12*, 155–176.

[34] Li, Y. F.; Chen, X. Y.; Wang, R. X.; Zhou, N.; Huang, F.; Zhao, J.; Su, Z. H.; Chen, S.; Liang, G. X. Defect-level trap optimization in $Cu_2ZnSn(S,Se)_4$ photovoltaic materials via Sb^{3+}-doping for over 13% efficiency solar cells. *J. Mater. Chem. A* **2024**, *12*, 10260–10268.

[35] Tang, R.; Chen, S.; Zheng, Z. H.; Su, Z. H.; Luo, J. T.; Fan, P.; Zhang, X. H.; Tang, J.; Liang, G. X. Heterojunction annealing enabling record open-circuit voltage in antimony triselenide solar cells. *Adv. Mater.* **2022**, *34*, 2109078.

[36] Chen, X. Y.; Ishaq, M.; Ahmad, N.; Tang, R.; Zheng, Z. H.; Hu, J. G.; Su, Z. H.; Fan, P.; Liang, G. X.; Chen, S. Ag, Ti dual-cation substitution in $Cu_2ZnSn(S,Se)_4$ induced growth promotion and defect suppression for high-efficiency solar cells. *J. Mater. Chem. A* **2022**, *10*, 22791–22802.

[37] Chen, X. Y.; Zhao, Y. H.; Ahmad, N.; Zhao, J.; Zheng, Z. H.; Su, Z. H.; Peng, X. G.; Li, X. J.; Zhang, X. H.; Fan, P. et al. Achieving high open-circuit voltage in efficient kesterite solar cells via lanthanide europium ion induced carrier lifetime enhancement. *Nano Energy* **2024**, *124*, 109448.

[38] Zhong, X. Y.; Wang, J. L.; Han, L. T.; Chi, J. J.; Liu, T.; Kou, D. X.; Zhou, W. H.; Zhou, Z. J.; Yuan, S. J.; Meng, Y. N. et al. Li, Ag Co-doping enables efficient kesterite solar cell with a high fill factor of 74.30%. *Adv. Funct. Mater.* **2025**, *35*, 2418548.

[39] Cui, C. C.; Kou, D. X.; Zhou, W. H.; Zhou, Z. J.; Yuan, S. J.; Qi, Y. F.; Zheng, Z.; Wu, S. X. Surface defect ordered $Cu_2ZnSn(S,Se)_4$ solar cells with efficiency over 12% via manipulating local substitution. *J. Energy Chem.* **2022**, *67*, 555–562.

[40] Wang, M. Y.; Geng, H.; Zhu, J. C.; Cui, Y. B.; Zhao, S. H.; Fu, J. J.; Kou, D. X.; Sun, J.; Zhao, C. L.; Wu, S. X. et al. Hyperactive selenium source yields kesterite solar cells with 12.86% efficiency. *Adv. Funct. Mater.* **2023**, *33*, 2307389.

[41] Liang, G. X.; Li, C. H.; Zhao, J.; Fu, Y.; Yu, Z. X.; Zheng, Z. H.; Su, Z. H.; Fan, P.; Zhang, X. H.; Luo, J. T. et al. Self-powered broadband kesterite photodetector with ultrahigh specific detectivity for weak light applications. *SusMat* **2023**, *3*, 682–696.

[42] Deng, S. C.; Wang, S. F.; Wang, Y. Y.; Xiao, Q.; Meng, Y. N.; Kou, D. X.; Zhou, W. H.; Zhou, Z. J.; Zheng, Z.; Wu, S. X. Impact of oxygen incorporation on interface optimization and defect suppression for efficiency enhancement in $Cu_2ZnSn(S,Se)_4$ solar cells. *J. Energy Chem.* **2024**, *95*, 77–85.

[43] Mao, Y.; Wang, T.; Jian, Y.; Huang, Y. Y.; Deng, Y. M.; Gu, E. N.; Lin, X. Z.; Yang, G. W. 12.86% efficient $Cu_2ZnSn(S,Se)_4$ thin film solar cells via inkjet printing with 2-methoxyethanol-based air-stable precursor ink. *Adv. Funct. Mater.* **2025**, *35*, 2416689.

[44] Duan, B. W.; Guo, L. B.; Yu, Q.; Shi, J. J.; Wu, H. J.; Luo, Y. H.; Li, D. M.; Wu, S. X.; Zheng, Z.; Meng, Q. B. Highly efficient solution-processed CZTSSe solar cells based on a convenient sodium-incorporated post-treatment method. *J. Energy Chem.* **2020**, *40*, 196–203.

[45] Wang, J. L.; Zhou, J. Z.; Xu, X.; Meng, F. Q.; Xiang, C. X.; Lou, L. C.; Yin, K.; Duan, B. W.; Wu, H. J.; Shi, J. J. et al. Ge bidirectional diffusion to simultaneously engineer back interface and bulk defects in the absorber for efficient cztsse solar cells. *Adv. Mater.* **2022**, *34*, 2202858.

[46] Deng, Y. Q.; Zhou, Z. J.; Zhang, X.; Cao, L.; Zhou, W. H.; Kou, D. X.; Qi, Y. F.; Yuan, S. J.; Zheng, Z.; Wu, S. X. Adjusting the SnZn defects in $Cu_2ZnSn(S,Se)_4$ absorber layer via Ge^{4+} implanting for efficient kesterite solar cells. *J. Energy Chem.* **2021**, *61*, 1–7.

[47] Guillén, E.; Ramos, F. J.; Anta, J. A.; Ahmad, S. Elucidating transport-recombination mechanisms in perovskite solar cells by small-perturbation techniques. *J. Phys. Chem. C* **2014**, *118*, 22913–22922.

[48] Wang, S. Y.; Zhao, Y. Q.; Yao, L. Q.; Li, C.; Gong, J. B.; Chen, G. L.; Li, J. M.; Xiao, X. D. Efficient and stable all-inorganic $Sb_2(S,Se)_3$ solar cells via manipulating energy levels in MnS hole transporting layers. *Sci. Bull.* **2022**, *67*, 263–269.

[49] Liu, D.; Tang, R. F.; Ma, Y. Y.; Jiang, C. H.; Lian, W. T.; Li, G.; Han, W. H.; Zhu, C. F.; Chen, T. Direct hydrothermal deposition of antimony triselenide films for efficient planar heterojunction solar cells. *ACS Appl. Mater. Interfaces* **2021**, *13*, 18856–18864.